

## Accepted Manuscript

Title: Synthesis of NiO@MnO<sub>2</sub> core/shell nanocomposites for supercapacitor application

Author: Junjiao Chen Ying Huang Chao Li Xuefang Chen  
Xiang Zhang



PII: S0169-4332(15)02606-9  
DOI: <http://dx.doi.org/doi:10.1016/j.apsusc.2015.10.187>  
Reference: APSUSC 31668

To appear in: *APSUSC*

Received date: 15-6-2015  
Revised date: 12-10-2015  
Accepted date: 26-10-2015

Please cite this article as: J. Chen, Y. Huang, C. Li, X. Chen, X. Zhang, Synthesis of NiO@MnO<sub>2</sub> core/shell nanocomposites for supercapacitor application, *Applied Surface Science* (2015), <http://dx.doi.org/10.1016/j.apsusc.2015.10.187>

This is a PDF file of an unedited manuscript that has been accepted for publication. As a service to our customers we are providing this early version of the manuscript. The manuscript will undergo copyediting, typesetting, and review of the resulting proof before it is published in its final form. Please note that during the production process errors may be discovered which could affect the content, and all legal disclaimers that apply to the journal pertain.

- MnO<sub>2</sub> nanosheets were grown on the surface of porous NiO microtube.
- The NiO@MnO<sub>2</sub> nanocomposite exhibits excellent cycle performance.
- The nanocomposite exhibits specific capacitance of 266.7 F g<sup>-1</sup> at 0.5 A g<sup>-1</sup>

## Synthesis of NiO@MnO<sub>2</sub> core/shell nanocomposites for supercapacitor application

Junjiao Chen, Ying Huang\*, Chao Li, Xuefang Chen and Xiang Zhang

Department of Applied Chemistry and The Key Laboratory of Space Applied Physics and Chemistry, Ministry of Education, School of Science, Northwestern Polytechnical University, Xi'an 710072, PR China

**Abstract:** In this work, NiO@MnO<sub>2</sub> core/shell nanocomposites were fabricated by a two-step method. The morphology and structure of the nanocomposites were characterized by scanning electron microscopy, transmission electron microscopy, X-ray photoelectron spectroscopy, X-ray diffraction analysis and thermal gravity analysis. In addition, the supercapacitive performances were examined by cyclic voltammogram (CV), galvanostatic charge-discharge and electrochemical impedance spectroscopy (EIS). The electrochemical results indicate that the composite exhibits a specific capacitance of 266.7 F g<sup>-1</sup> at 0.5 A g<sup>-1</sup> and excellent cycling stability (81.7% retention after 2000 cycles at 1 A g<sup>-1</sup>). Therefore, this work offers meaningful reference for supercapacitor applications in the future.

Keywords: NiO tube; MnO<sub>2</sub> nanosheets; supercapacitor; nanocomposites

---

\* Corresponding author. Tel.+862988431636.

Email addresses: chenjunjiao001@163.com, yingh@nwpu.edu.cn (Y.Huang).

## 1. Introduction

As a kind of energy storage device, supercapacitors (SCs) have its unique properties, such as high power density, fast charge–discharge rate and stable cycling performance[1]; SCs have been received great attention with the development of electric car industry in recent years. Generally, there are two type of storage energy mechanism for supercapacitors: one is ion adsorption (electrical double-layer capacitors, EDLCs), the other is fast surface redox reactions (pseudocapacitors). Potentially, pseudocapacitors can provide much higher capacitance values than EDLCs through Faradic reaction[2]. Up to now, transition metal oxides with variable valence have been widely used in pseudocapacitors, such as NiO[3], MnO<sub>2</sub>[4], Co<sub>3</sub>O<sub>4</sub> [5], and NiCo<sub>2</sub>O<sub>4</sub>[6].

Nickel oxide (NiO) is widely investigated as one of the most promising pseudocapacitive materials which owns unusually high theoretical specific capacitance (2573 F g<sup>-1</sup>)[7] and excellent electrochemical reaction reactivity. The morphology of NiO and its controlled synthesis have large impact on its electrochemical performance because morphology is closely related to the specific surface area, a variety of porous nanostructures with large surface areas have been synthesized via surfactant-template, sol-gel, anodization and hard template methods[8]. MnO<sub>2</sub>, an important pseudocapacitive material, has many intriguing characteristics including high theoretical specific capacitance (1370 F g<sup>-1</sup>), natural abundance, low cost, environmental friendly and rich redox activity[9]. Unfortunately, the practical applications of MnO<sub>2</sub> are limited due to its weak rate capability and cycling stability, which can be attributed to its poor electrical conductivity[10, 11].

Meanwhile, binary metal oxide composites such as Co<sub>3</sub>O<sub>4</sub>@NiCo<sub>2</sub>O<sub>4</sub>[12], NiCo<sub>2</sub>O<sub>4</sub>@NiO[13], Co<sub>3</sub>O<sub>4</sub>@NiMoO<sub>4</sub>[14] and NiCo<sub>2</sub>O<sub>4</sub>@NiCo<sub>2</sub>O<sub>4</sub>[15] also have received much attention as supercapacitor electrode materials. Pseudocapacitive material core-pseudocapacitive material shell

presents another intriguing core-shell design because both core and shell materials have redox reactions during charge and discharge processes, which results in high specific capacitances [16]. These materials have multiple oxidation states and structures that enable multiple redox reactions and have been reported to exhibit a higher performance than single component oxides, and binary metal oxide with core/shell structure have short ion transport pathways, superior electron collection efficiency and multifunctionalities of components. Thus, it is highly promising to design core/shell structure, in which each component's properties could be optimized [17].

In this present work, a novel binary metal oxide NiO@MnO<sub>2</sub> core/shell nanocomposites were fabricated by a two-step method. NiO microtubes are obtained by calcination treatment of Ni(dmgl)<sub>2</sub> (dimethylglyoxime = dmgl) nanorod, then MnO<sub>2</sub> nanosheets were grown on the surface of NiO microtubes by hydrothermal method. NiO microtubes are the "core", MnO<sub>2</sub> nanosheets are the "shell". To the best of our knowledge, such a unique NiO@MnO<sub>2</sub> core/shell nanostructure has been never reported before. By virtue of the synergetic contribution from individual constituents and the sophisticated configuration, the resulting nanocomposites exhibited high specific capacitance with high cycling stability when applied as supercapacitor electrode materials.

## **2. Experimental**

### **2.1 Synthesis of NiO porous microtubes**

All reagents were of analytical grade and used as received without further purification. Firstly, 19.2 g polyethylene glycol and 1.16 g dimethylglyoxime (dmgl) were dissolved in 200 mL of absolute ethanol, and then 200 mL of 0.01 M nickel chloride solution were poured into above-mentioned solution under vigorous stirring, and keep this red mixture at 0 °C for 12 h. The precursor was collected by filtration and washed with large amount of water and absolute ethanol

and dried in a vacuum oven at 60 °C over night. Then the red product was calcined at 500 °C for 3 h in a muffle furnace to obtain NiO microtubes.

## 2.2 Synthesis of NiO@MnO<sub>2</sub>

The prepared 60 mg NiO microtubes were dispersed in 20 mL deionized water by vigorous stirring, then 60 ml of 0.02 M KMnO<sub>4</sub> solution was mixed with this dispersion. After stirring for 1h, the mixture solution was transferred into a 100 mL Teflon-lined stainless-steel autoclave, the autoclave was heated at 120 °C for 12 h and then cooled to room temperature naturally. The as-obtained black precipitate was collected by filtration and washed with deionized water for several times. The resulting final product was dried at 60 °C for 12 h.

## 2.3 Structural characterization

The structure of the fabricated samples was examined by X-ray diffraction analysis (XRD) (Rigaku, model D/max-2500 system at 40 kV and 100 mA of Cu K $\alpha$ ). The X-ray photoelectron spectroscopy (XPS) spectra were tested by an ESCALab 250 electron spectrometer (Thermo Scientific Corporation). Thermo gravimetric analysis (TGA, Q500) was conducted with a heating rate of 10 °C min<sup>-1</sup>. The surface morphology of the composites was investigated by scanning electron microscope (SEM, VEGA 3, The Czech Republic, TESCAN) and a model field emission transmission electron microscope (FETEM, USA, Tecnai F30 G2 FEI CO.).

## 2.4 Electrochemical measurements

The working electrode materials were prepared by mixing the obtained sample, acetylene black and polytetrafluoroethylene (PTFE) in a mass ratio of 80:10:10. The hybrid was mixed with ethanol for homogeneity and then coated on nickel foam substrates (1cm×1cm) as the working electrode and dried at 60 °C for 8 h; the as-formed electrodes loaded with the hybrid were then

pressed at 10 MPa for 60s and then further dried at 80 °C overnight before using. The typical mass loading of the sample in each electrode is about 8 mg. Electrochemical measurements were performed on an Autolab Electrochemical Workstation (PGSTAT302N) by the three-electrode system, Platinum electrode and the standard calomel electrode (SCE) were used as the counter and reference electrodes respectively. 2 M KOH solution was served as the electrolyte at room temperature. Cyclic voltammogram (CV) was recorded between 0 and 0.45 V at scan rates ranging from 1 to 20 mV/s. Galvanostatic charge/discharge testing was conducted at different current densities from 0.5 to 15 Ag<sup>-1</sup> between 0 and 0.4 V. The electrochemical impedance spectroscopy (EIS) measurements were performed in a frequency range from 10<sup>-2</sup> Hz to 100 kHz with potential amplitude of 5 mV.

### 3. Results and discussion

NiO@MnO<sub>2</sub> core/shell nanocomposites are fabricated by a two-step method, as shown in Fig.1(a), the NiO microtubes were fabricated by the calcination of Ni(dmg)<sub>2</sub> microtubes, and then MnO<sub>2</sub> nanosheets were grown on the surface of NiO microtubes by hydrothermal method. Fig.1(b) shows the SEM image of Ni(dmg)<sub>2</sub> nanorods, indicating Ni(dmg)<sub>2</sub> has a one-dimensional morphology, the length and diameter of the straight nanorod is about 30~50 μm and 0.5~1 μm respectively. After the calcination of nanorod precursors, the NiO microtubes are formed. Fig.1 (c) and Fig.1 (d) disclose the morphology of NiO microtubes, and the image (right-inset in Fig 1(c)) demonstrates that the NiO sample has tube-like nanostructures, and porous structure of NiO microtube can be clear seen in the Fig.1 (d). As shown in Fig.1 (e) and Fig.1 (f), a layer of MnO<sub>2</sub> nanosheets were grown on the surface of NiO tube after hydrothermal reaction in KMnO<sub>4</sub> solution for 6 h. The tube-like nanostructures of NiO is still well retained even after the MnO<sub>2</sub> nanosheets

decorated on the surface. A representative HRTEM image (Fig.1 (g)) shows that the measured interplanar distance is 0.475 nm, this d-space consistent with the (111) plane of the cubic  $\text{MnO}_2$ . The SAED patterns (inset in Fig.1 (g)) with well-defined rings also demonstrate the crystalline feature of  $\text{NiO@MnO}_2$ . EDS (Fig.1 (h)) demonstrates that Ni, Mn, O elements were contained, indicating the formation of  $\text{NiO@MnO}_2$ , which is consistent with the XPS data.

The crystal structure and purity are determined by XRD technique. Fig.2 (a) shows the XRD patterns of NiO and  $\text{NiO@MnO}_2$  samples. For the NiO sample, the prominent diffraction peaks appeared at  $2\theta$  of  $37.3^\circ$ ,  $43.3^\circ$ ,  $62.9^\circ$ ,  $75.4^\circ$ ,  $79.4^\circ$ , and all strong diffraction peaks can be indexed to the standard data of the crystal structure of NiO (JCPDS No.78-0643), no irrelevant peaks are detectable, indicating the high purity of NiO. It can be seen that the diffraction peaks of the  $\text{NiO@MnO}_2$  core-shell nanocomposites are almost in accord with the standard XRD pattern of NiO (JCPDS No.78-0643), and the first two peaks at  $12.3^\circ$  and  $18.7^\circ$  can be attributed to the  $\text{MnO}_2$  (JCPDS No.18-0802), indicating the formation of  $\text{NiO@MnO}_2$  nanocomposites or the products are the mixture of NiO and  $\text{MnO}_2$ .

Thermogravimetric (TG) measurements were carried out to determine the anneal process of  $\text{Ni(dmg)}_2$ . Fig.2 (b) shows the TG curves of  $\text{Ni(dmg)}_2$ , it can be seen that the weight loss is about 74% at about  $300^\circ\text{C}$ , which is attributed to the transformation from  $\text{Ni(dmg)}_2$  to NiO. Obviously,  $\text{H}_2\text{O}$ ,  $\text{CO}_2$ ,  $\text{CO}$ ,  $\text{N}_2$ ,  $\text{NO}_x$  are released during the thermal decomposition[18]. After  $380^\circ\text{C}$ , the TG traces are stable with no further weight loss.

Elemental composition and chemical states are further investigated by XPS in Fig.3. The survey spectrum (Fig.3 (a)) demonstrates that the products were composed of Ni, Mn, O elements, the high-resolution spectrum of O 1s, Ni 2p, Mn 2p are exhibited in the Fig (b-d). The O 1s spectrum

is shown in Fig.3 (b), three main peaks at 529.9, 531.3 and 532.1 eV are attributable to metal–oxygen bonds (M-O-M), metal-hydroxide (M-OH), and water (H-O-H) on the surface, respectively[19]. The Ni 2p spectrum, as shown in Fig.3 (c), consists of one spin-orbit doublets characteristic of Ni<sup>2+</sup> and two shakeup satellites, the two peaks at binding energy of 854.6 eV and 872.1 eV are assigned to Ni<sup>2+</sup>[20], while the satellite peaks at 879.0 eV and 860.8 eV are two shake-up type peaks of the nickel at the high binding energy sides of the Ni 2p<sub>1/2</sub> and Ni 2p<sub>3/2</sub> edge [21]. The Mn 2p spectrum exhibits multiple splitting with two main peaks centered at 642.4 eV and 654.0 eV, which can be attributed to Mn 2p<sub>3/2</sub> and Mn 2p<sub>1/2</sub> of Mn<sup>4+</sup> in MnO<sub>2</sub>, respectively, and the spin-energy separation is 11.6 eV [22, 23]. Moreover, Mn<sup>3+</sup> and Mn<sup>5+</sup> species are also detected in the spectrum. However, the intensities of this two peaks are much weaker than those for Mn<sup>4+</sup>, demonstrating that element Mn in NiO@MnO<sub>2</sub> is presented in the dominant chemical state of Mn<sup>4+</sup> [24].

A detailed measurement of the electrochemical performance of NiO@MnO<sub>2</sub> nanocomposites are shown in Fig.4. CV curves of NiO@MnO<sub>2</sub> are shown in the Fig.4 (a) at different scan rates in a fixed potential range of -0.1~0.45 V (vs.SCE) in 2 M aqueous KOH electrolyte. A pair of well-defined redox peaks is obviously observed in all CV curves, suggesting the typical pseudocapacitive feature of active materials, which is obviously different from the electric double-layer capacitance characterized by nearly rectangular CV curves, the redox couples correspond to the reversible reactions of and Ni<sup>2+</sup>/Ni<sup>3+</sup> transitions. The shape of the CV curves barely changes, indicating that the electrode have a good rate capability. To further investigate the electrochemical performance of the NiO@MnO<sub>2</sub> electrode, we perform galvanostatic charge–discharge (GCD) curves (Fig.4b) at various current densities in a fixed potential range of

0~0.4 V (vs.SCE). The shape of charge-discharge curves is basically symmetric, suggesting good reversibility redox processes. Voltage plateaus at around 0.28 V and 0.21 V can be seen in the charge and discharge process respectively. The specific capacitances of the NiO@MnO<sub>2</sub> are 266.7, 253.3, 218.3, 181.7, 168.3, 147.3 F g<sup>-1</sup> at current densities of 0.5, 1, 2, 4, 6, 8, 10 A g<sup>-1</sup>. CV curves have been made comparison between NiO@MnO<sub>2</sub> and NiO at 10 mv/s in the Fig.4(c), it can be clearly seen that the CV curve of NiO@MnO<sub>2</sub> electrode shows the higher integrated area than NiO electrodes, furthermore, it also can be clearly seen that the GCD curves (Fig.3d) of NiO@MnO<sub>2</sub> electrode shows the higher discharge time than NiO electrodes, indicating the higher specific capacitance of NiO@MnO<sub>2</sub> nanocomposites due to the optimal core-shell structure and the introduction MnO<sub>2</sub>.

As shown in Fig.4 (e), contrasting with the specific capacitances of NiO@MnO<sub>2</sub> and NiO electrode at various charge/discharge current, the capacitance of NiO@MnO<sub>2</sub> reduces from 266.7 F g<sup>-1</sup> ( current density of 0.5 A g<sup>-1</sup> ) to 120 F g<sup>-1</sup> ( current density of 15 A g<sup>-1</sup> ) with 45% of the specific capacitance remaining, in the same process, the capacitance of NiO electrode reduces from 94 F g<sup>-1</sup> ( current density of 0.5 A g<sup>-1</sup> ) to 52 F g<sup>-1</sup> ( current density of 15 A g<sup>-1</sup> ) with 55% of the specific capacitance remaining, and the capacitance of MnO<sub>2</sub> electrode reduces from 213 F g<sup>-1</sup> ( current density of 0.5 A g<sup>-1</sup> ) to 81 F g<sup>-1</sup> ( current density of 15 A g<sup>-1</sup> ) with 38% of the specific capacitance remaining. This result indicates that the specific capacitance of NiO and MnO<sub>2</sub> electrode are both much lower than NiO@MnO<sub>2</sub> electrode. The higher specific capacitance of NiO@MnO<sub>2</sub> electrode is due to ultrathin MnO<sub>2</sub> nanosheets were well wrapped on the surface of NiO microtubes to form a highly porous structure, the porous nanoarchitecture and MnO<sub>2</sub> nanosheets provides the composites with larger surface area that means a large

electrode/electrolyte contact interface and more active sites for electrochemical reactions. We further studied the cycling performance (Fig.4 (f)) of the electrodes at  $1 \text{ A g}^{-1}$ , the capacity retention (81.7%) of NiO@MnO<sub>2</sub> electrode shows higher than that of NiO electrode (77.4%) and MnO<sub>2</sub> electrode (73.5%) after 2000 charge-discharge cycles, the cycling performance of NiO@MnO<sub>2</sub> is very excellent because the core/shell structure is stable during repeated charge-discharge process.

To further understand the fundamental electrochemical behavior of NiO@MnO<sub>2</sub> composites, EIS data of NiO, MnO<sub>2</sub> and NiO@MnO<sub>2</sub> electrode are shown in Fig.5(a). The impedance spectra display similar form with a semicircle at a high-frequency region and a straight line at low-frequency region. The intersection of the plot at the x-axis represents  $R_s$  of the electrochemical system, which contains three sections: the intrinsic resistance of the substrate, the resistance of the electrolyte and the contact resistance at the interface between active materials and current collector[25], the  $R_s$  value of NiO@MnO<sub>2</sub> ( $0.186 \Omega$ ) is bigger than that of NiO ( $0.120 \Omega$ ), but which is smaller than that of MnO<sub>2</sub> ( $0.373\Omega$ ).  $R_{ct}$  stands for charge transfer resistance between the electrode and the electrolyte[26], which corresponding to the diameter of a semicircle, the  $R_{ct}$  value of NiO@MnO<sub>2</sub> ( $0.235 \Omega$ ) is much bigger than that of NiO ( $0.065 \Omega$ ), but which is also smaller than that of MnO<sub>2</sub> ( $0.373\Omega$ ). The slope of the straight line is related to the Warburg impedance ( $R_w$ ) which represents the electrolyte diffusion in the active materials[27], the higher is the slope the easier is the ion diffusion/adsorption process, Warburg impedance is reduced when the slope is increased, a line with large slope at low frequency illustrates that the ion diffusion in the solution and the adsorption of ions onto the electrode surface occur swiftly, the  $R_w$  value of NiO@MnO<sub>2</sub> is higher than that of that of NiO, but which is smaller than that of MnO<sub>2</sub>. These

results indicate the introduction of poor conductivity  $\text{MnO}_2$  lead to increase the solution resistance, the charge transfer resistance and the Warburg impedance decrease. In fact, this is the reason why the rate capability of  $\text{NiO@MnO}_2$  electrode is inferior to  $\text{NiO}$  electrode. Moreover, we also calculate the specific capacitance  $\text{NiO}$ ,  $\text{MnO}_2$ ,  $\text{NiO@MnO}_2$  from EIS data according to

$$C = \frac{1}{2\pi fZ''m}$$

where  $f$  is the operating frequency (Hz),  $Z''$  is the imaginary parts of the total device resistance (Ohm), and  $m$  is the mass of active materials in each electrode[28,29]. The result is shown in Fig.5(b), the capacitance of them is high at low frequency, and it start to decrease with the increasing frequency.

### conclusion

In summary, we have successfully synthesized  $\text{NiO@MnO}_2$  core/shell nanocomposites with distinct morphologies by a facile and scalable strategy.  $\text{NiO@MnO}_2$  nanocomposites show a high specific capacitance of  $266.7 \text{ F g}^{-1}$  at  $0.5 \text{ A g}^{-1}$ , excellent rate capability and remain at 81.7% of initial capacitance after 2000 cycles at  $1 \text{ A g}^{-1}$ . These results indicate that this kind of composites with excellent electrochemical properties can be a promising electrode material for supercapacitors.

### Acknowledgments

This work was supported by the Research Fund for the Doctoral Program of Higher Education of China under Grant no. 20136102110046, the Innovation Foundation of Shanghai Aerospace Science and Technology Grant no. SAST201373 and the Graduate Starting Seed Fund of Northwestern Polytechnical University (2015).

## References

- [1] Z. Yu, M. McInnis, J. Calderon, S. Seal, L. Zhai, J. Thomas, Functionalized graphene aerogel composites for high-performance asymmetric supercapacitors, *Nano Energy*, 11 (2015) 611-620.
- [2] Z. Li, High-performance solid-state supercapacitors based on graphene-ZnO hybrid nanocomposites, *Nanoscale Res. Lett.*, 8 (2013) 11479-11487.
- [3] G. Zhang, L. Yu, H.E. Hoster, X.W. Lou, Synthesis of one-dimensional hierarchical NiO hollow nanostructures with enhanced supercapacitive performance, *Nanoscale*, 5 (2013) 877-881.
- [4] F. Li, Y. Xing, M. Huang, K.L. Li, T.T. Yu, Y.X. Zhang, D. Losic, MnO<sub>2</sub> nanostructures with three-dimensional (3D) morphology replicated from diatoms for high-performance supercapacitors, *J. Mater. Chem. A*, 3 (2015) 7855-7861.
- [5] Y. Wang, Y. Lei, J. Li, L. Gu, H. Yuan, D. Xiao, Synthesis of 3D-nanonet hollow structured Co<sub>3</sub>O<sub>4</sub> for high capacity supercapacitor, *ACS Appl. Mater. Interfaces*, 6 (2014) 6739-6747.
- [6] E. Jokar, A. zad, S. Shahrokhian, Synthesis and characterization of NiCo<sub>2</sub>O<sub>4</sub> nanorods for preparation of supercapacitor electrodes, *J. Solid State Electrochem.*, 19 (2015) 269-274.
- [7] J. Liu, J. Jiang, M. Bosman, H.J. Fan, Three-dimensional tubular arrays of MnO<sub>2</sub>-NiO nanoflakes with high areal pseudocapacitance, *J. Mater. Chem.*, 22 (2012) 2419-2426.
- [8] S.I. Kim, J.S. Lee, H.J. Ahn, H.K. Song, J.H. Jang, Facile route to an efficient NiO supercapacitor with a three-dimensional nanonetwork morphology, *ACS Appl. Mater. Interfaces*, 5 (2013) 1596-1603.
- [9] Z. Yu, B. Duong, D. Abbitt J. Thomas, Highly ordered MnO<sub>2</sub> nanopillars for enhanced supercapacitor performance, *Adv. Mater.*, 25 (2013) 3302-3306.

- [10] L. Li, Z.A. Hu, N. An, Y.Y. Yang, Z.M. Li, H.Y. Wu, Facile Synthesis of  $\text{MnO}_2/\text{CNTs}$  Composite for Supercapacitor Electrodes with Long Cycle Stability, *J. Phys. Chem. C*, 118 (2014) 22865-22872.
- [11] Z. Yu, J. Thomas, Energy storing electrical cables: Integrating energy storage and electrical conduction, *Adv. Mater.*, 26 (2014) 4279-4285.
- [12] X. Gao, Y. Zhang, M. Huang, F. Li, C. Hua, L. Yu, H. Zheng, Facile synthesis of  $\text{Co}_3\text{O}_4@ \text{NiCo}_2\text{O}_4$  core-shell arrays on Ni foam for advanced binder-free supercapacitor electrodes, *Ceram Int*, 40 (2014) 15641-15646.
- [13] W. Yang, Z. Gao, J. Ma, X. Zhang, J. Wang, J. Liu, Hierarchical  $\text{NiCo}_2\text{O}_4@ \text{NiO}$  core-shell hetero-structured nanowire arrays on carbon cloth for a high-performance flexible all-solid-state electrochemical capacitor, *J. Mater. Chem. A*, 2 (2014) 1448-1457.
- [14] D. Cai, D. Wang, B. Liu, L. Wang, Y. Liu, H. Li, Y. Wang, Q. Li, T. Wang, Three-Dimensional  $\text{Co}_3\text{O}_4@ \text{NiMoO}_4$  Core/Shell Nanowire Arrays on Ni Foam for Electrochemical Energy Storage, *ACS Appl. Mater. Interfaces*, 6 (2014) 5050-5055.
- [15] X. Liu, S. Shi, Q. Xiong, L. Li, Y. Zhang, H. Tang, C. Gu, X. Wang, J. Tu, Hierarchical  $\text{NiCo}_2\text{O}_4@ \text{NiCo}_2\text{O}_4$  core/shell nanoflake arrays as high-performance supercapacitor materials, *ACS Appl. Mater. Interfaces*, 5 (2013) 8790-8795.
- [16] Z. Yu, L. Tetard, L. Zhai, J. Thomas, Supercapacitor electrode materials: Nanostructures from 0 to 3 dimensions, *Energy Environ. Sci.*, 8 (2015) 702-730.
- [17] M. Huang, F. Li, Y.X. Zhang, B. Li, X. Gao, Hierarchical NiO nanoflake coated CuO flower core-shell nanostructures for supercapacitor, *Ceram. Int.*, 40 (2014) 5533-5538.

- [18] N. Wang, L. Chen, X. Ma, J. Yue, F. Niu, H. Xu, J. Yang, Y. Qian, Facile synthesis of hierarchically porous NiO micro-tubes as advanced anode materials for lithium-ion batteries, *J. Mater. Chem. A*, 2 (2014) 16847-16850.
- [19] M. Chigane, M. Ishikawa, Manganese oxide thin film preparation by potentiostatic electrolyses and electrochromism, *J. Electrochem. Soc.*, 147 (2000) 2246-2251.
- [20] Z. Liu, Q. Xu, J. Wang, N. Li, S. Guo, Y. Su, H. Wang, J. Zhang, S. Chen, Facile hydrothermal synthesis of urchin-like NiCo<sub>2</sub>O<sub>4</sub> spheres as efficient electrocatalysts for oxygen reduction reaction, *Int. J. Hydrogen Energy*, 38 (2013) 6657-6662.
- [21] J. Xiao, S. Yang, Bio-inspired synthesis of NaCl-type Co<sub>x</sub>Ni<sub>1-x</sub>O (0 [less-than-or-equal] x < 1) nanorods on reduced graphene oxide sheets and screening for asymmetric electrochemical capacitors, *J. Mater. Chem.*, 22 (2012) 12253-12262.
- [22] J. Yan, Z. Fan, T. Wei, W. Qian, M. Zhang, F. Wei, Fast and reversible surface redox reaction of graphene–MnO<sub>2</sub> composites as supercapacitor electrodes, *Carbon*, 48 (2010) 3825-3833.
- [23] H. Xia, M. Lai, L. Lu, Nanoflaky MnO<sub>2</sub>/carbon nanotube nanocomposites as anode materials for lithium-ion batteries, *J. Mater. Chem.*, 20 (2010) 6896-6902.
- [24] Y. Zhao, P. Jiang, MnO<sub>2</sub> nanosheets grown on the ZnO-nanorod-modified carbon fibers for supercapacitor electrode materials, *Colloids Surf., A*, 444 (2014) 232-239.
- [25] X. Xie, C. Zhang, M.-B. Wu, Y. Tao, W. Lv, Q.-H. Yang, Porous MnO<sub>2</sub> for use in a high performance supercapacitor: replication of a 3D graphene network as a reactive template, *Chem Commun*, 49 (2013) 11092-11094.

- [26] B. Yan, X. Li, Z. Bai, M. Li, L. Dong, D. Xiong, D. Li, Superior lithium storage performance of hierarchical porous vanadium pentoxide nanofibers for lithium ion battery cathodes, *J. Alloys Compd.*, 634 (2015) 50-57.
- [27] Y. Luo, H. Zhang, D. Guo, J. Ma, Q. Li, L. Chen, T. Wang, Porous NiCo<sub>2</sub>O<sub>4</sub>-reduced graphene oxide (rGO) composite with superior capacitance retention for supercapacitors, *Electrochim. Acta*, 132 (2014) 332-337.
- [28] I. Stepniak, A. Ciszewski, Grafting effect on the wetting and electrochemical performance of carbon cloth electrode and polypropylene separator in electric double layer capacitor, *J. Power Sources*, 195 (2010) 5130-5137.
- [29] J. Kang, J. Wen, S.H. Jayaram, A. Yu, X. Wang, Development of an equivalent circuit model for electrochemical double layer capacitors (EDLCs) with distinct electrolytes, *Electrochim. Acta*, 115 (2014) 587-598.

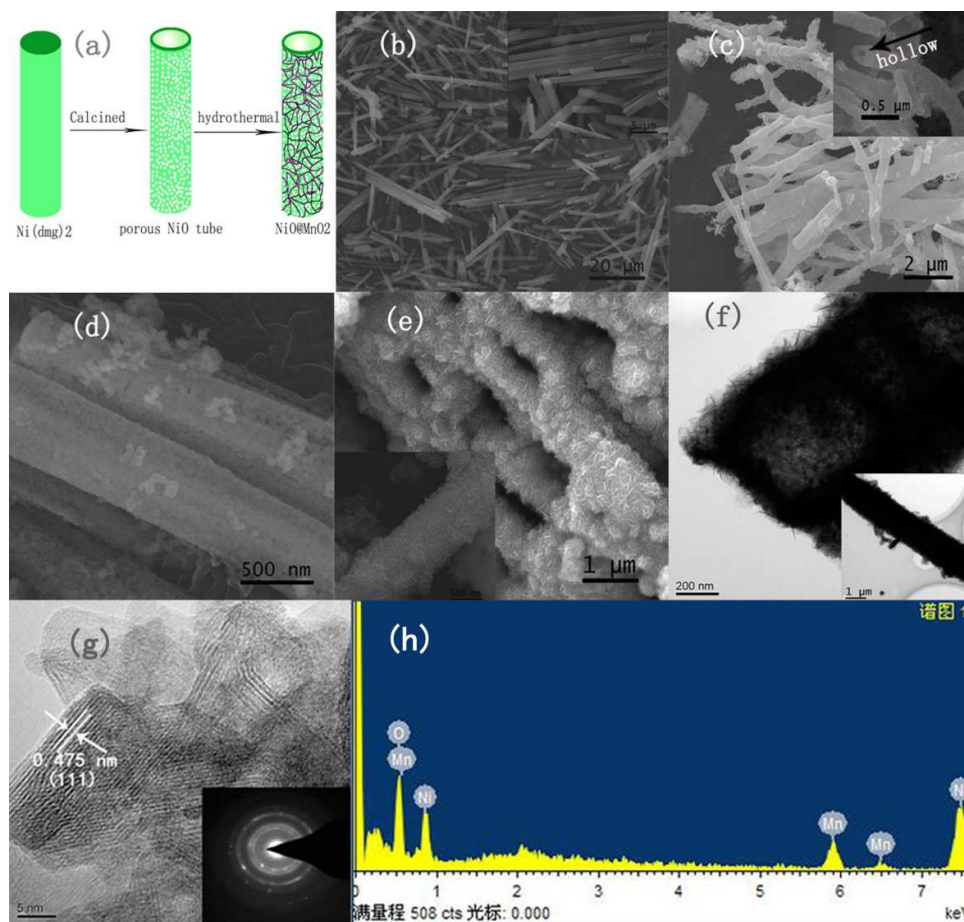


Fig.1 (a) Schematic illustration of the formation of NiO@MnO<sub>2</sub>. (b) SEM image of Ni(dmg)<sub>2</sub> and (c, d) NiO microtube, (e, f) SEM and TEM image of NiO@MnO<sub>2</sub>. (g) HRTEM image of NiO@MnO<sub>2</sub> and SEAD Pattern of NiO@MnO<sub>2</sub>. (g) Corresponding EDS spectrum of NiO@MnO<sub>2</sub>.

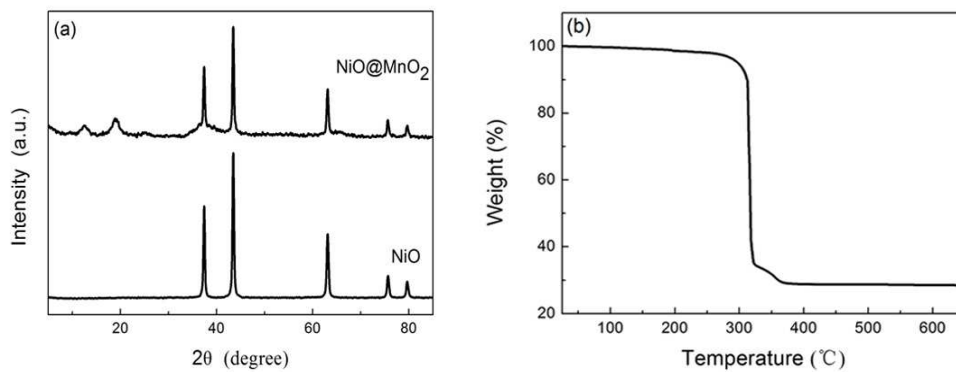


Fig.2 (a) XRD pattern of the NiO@MnO<sub>2</sub> nanocomposites, (b)TG Curve of Ni(dmg)<sub>2</sub> nanorod.

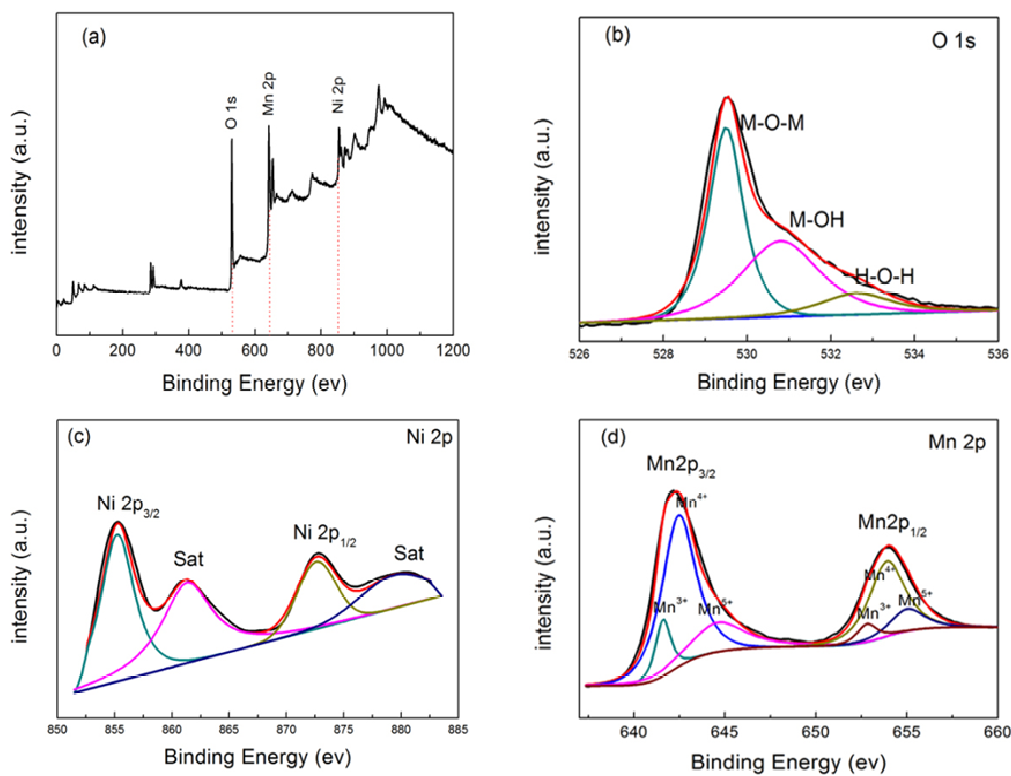


Fig.3 XPS spectra of (a) survey spectrum, (b)O 1s, (c)Ni 2p and (d) Mn 2p for NiO@MnO<sub>2</sub> nanocomposites.

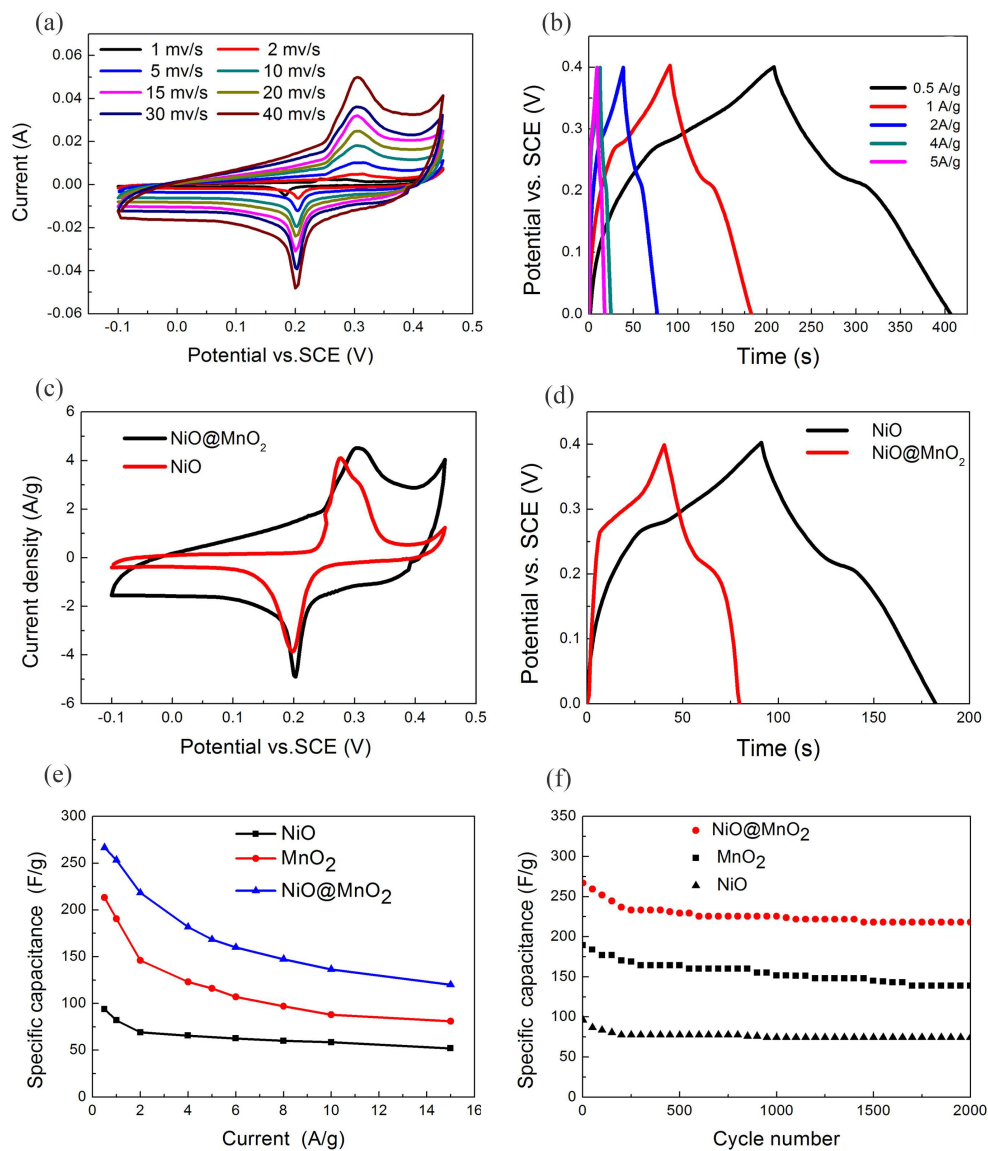


Fig.4 (a) Cyclic voltammetry curves of NiO@MnO<sub>2</sub> at various scan rates. (b) Galvanostatic charge/discharge curves of NiO@MnO<sub>2</sub> at different current densities. (c) CV curves of NiO@MnO<sub>2</sub> and NiO at 10mv/s. (d) Galvanostatic charge/discharge curves of NiO@MnO<sub>2</sub> and NiO at 1 A/g. (e) Specific capacitances of NiO@MnO<sub>2</sub>, MnO<sub>2</sub> and NiO electrodes at different current densities. (f) Cycling performance of the NiO@MnO<sub>2</sub>, MnO<sub>2</sub> and NiO electrodes at 1 A g<sup>-1</sup>.

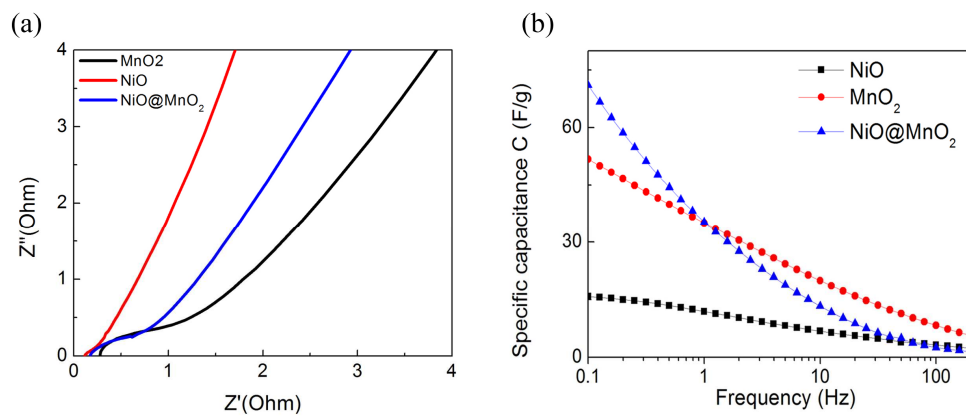
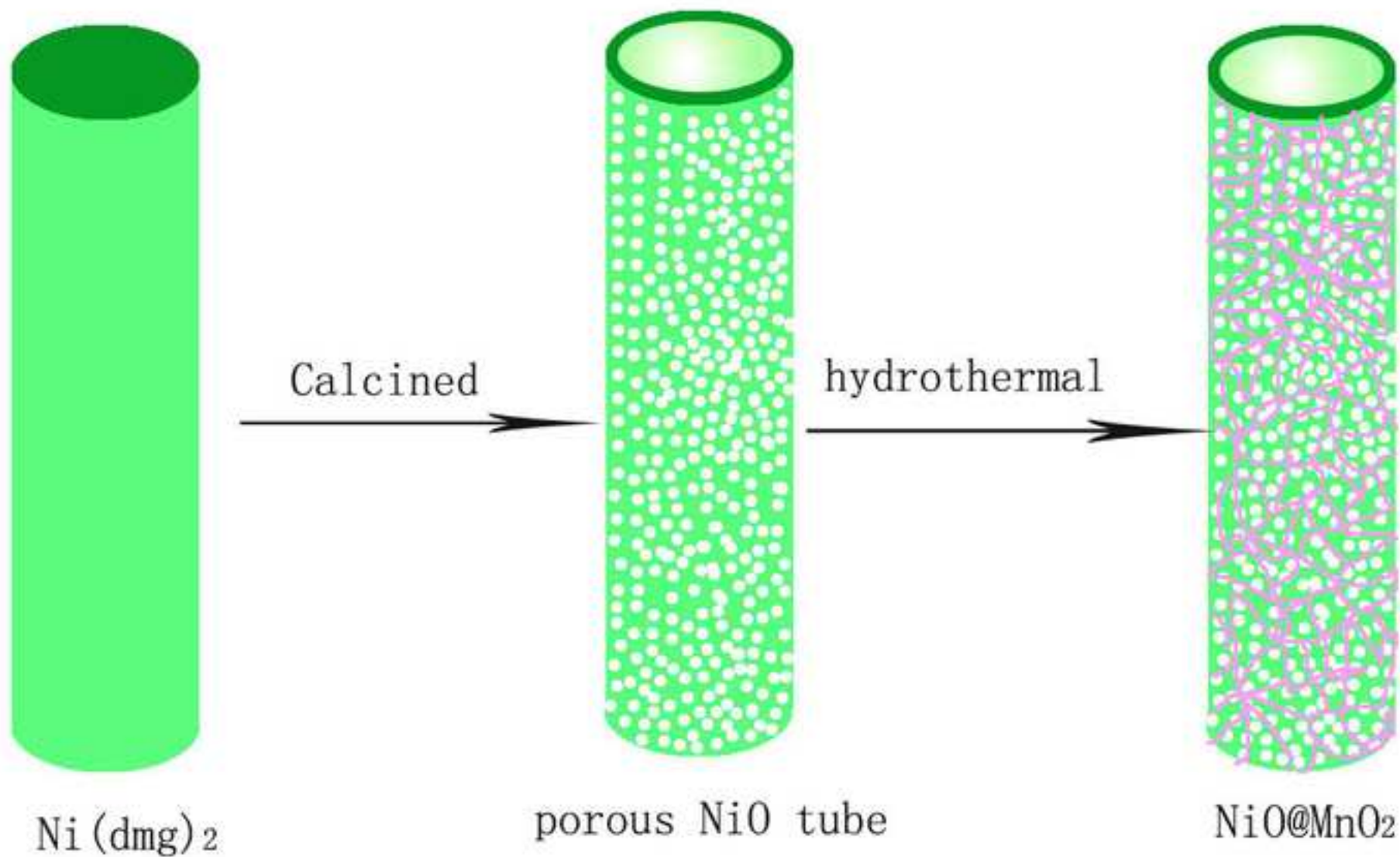


Fig.5(a) EIS data of  $NiO$ ,  $MnO_2$  and  $NiO@MnO_2$  electrode, (b) specific capacitance plot

vs. frequency of  $NiO$ ,  $MnO_2$  and  $NiO@MnO_2$  electrode.



# supercapacitor electrode materials